Exploring the Interfacial Structure and Crystallinity for Direct Growth of Mn_3Sn (0001) on Sapphire (0001) by Molecular Beam Epitaxy

Sneha Upadhyay[1,a], Tyler Erickson[1], Hannah Hall[1], Ashok Shrestha[1], David C. Ingram[1], Kai Sun[2], Juan Carlos Moreno Hernandez[3], Gregorio Hernandez Cocoletzi[3], Noboru Takeuchi[4], and Arthur R. Smith[1]

[1] *Nanoscale and Quantum Phenomena Institute, Department of Physics and Astronomy, Ohio University, Athens, OH 45701, USA.*

[2] *Michigan Center for Materials Characterization (MCMC) & Department of Materials Science and Engineering, The University of Michigan Ann Arbor, MI 48109, USA.*

[3] *Universidad Autónoma de Puebla, Instituto de Física, Apartado Postal J-48, Puebla 72570, México. and*

[4] *Centro de Nanociencias y Nanotecnología, Universidad Nacional Autónoma de México, Apartado Postal 14, Código Postal, Ensenada, Baja California 22800, México.*

(Dated: November 26, 2023)

[a] Corresponding Author : su196516@ohio.edu

Abstract

The Kagome antiferromagnet Mn_3Sn has garnered a lot of attention due to the presence of interesting properties such as anomalous Hall effects and Nernst effects. Until now, few papers have been reported to grow using molecular beam epitaxy with a buffer layer or on other substrates. In this paper, we discuss the synthesis of crystalline Mn_3Sn layers, prepared on Al_2O_3 (0001) without a buffer layer using molecular beam epitaxy. The growth is monitored *in-situ* using reflection high energy electron diffraction and measured *ex-situ* using X-ray diffraction, Rutherford back-scattering, and cross-sectional scanning transmission electron microscopy. The samples were deposited at 524 $\pm$ 5 °C, with an Mn: Sn atomic flux ratio of 3.2:1 for 90 minutes. Orientation relationships between the Mn_3Sn films and the sapphire substrates are determined from *in-plane* and *out-of-plane* measurements. Our analysis indicates that the resulting film is predominantly $c-$plane oriented. Lastly, the samples prepared in this way were found to be discontiguous, showing a 3-dimensional morphology. According to first-principles calculations, the Mn_3Sn exhibits a displaced Kagome structure in the very first stages of growth, for 2ML and 4ML growth on Al_2O_3 (0001). This result is corroborated by calculating the surface formation energies and explains the observed RHEED patterns.

Keywords: Kagome, Molecular beam epitaxy, surface formation energies

INTRODUCTION

Topological materials with kagome structures have garnered a lot of attention because of their physical properties in real and momentum space. These kagome structures have a broken time-reversal symmetry and large Berry curvature, which results in the rise of strong anomalous Hall effect (AHE) [1]. Recently, transition metal stannides are being extensively studied to probe these exotic properties of the kagome structures. For example, for CoSn and Fe_3Sn_2 kagome structures, topological flat bands and quasi-two-dimensional Dirac cones were observed respectively, using angle-resolved photoemission spectroscopy [1, 2]. Therefore, it is important to investigate the magnetic and electron transport properties of these kagome materials.

Moving forward, it would be interesting to have the possibility to tune the magnetic and topological properties and to achieve this, it is important to grow high-quality thin films. Several recent reports have shown the high-quality growth of kagome systems using molecular beam epitaxy (MBE). For example, using MBE, Hong *et al.* demonstrated the layered Kagome-structured growth of FeSn thin films on $LaAlO_3$ (111) substrates using MBE [3]. Then Cheng *et al.* reported the controlled growth of a superlattice consisting of Fe_3Sn_2 and Fe_3Sn using a modified method referred to by the authors as atomic layer MBE, demonstrating the ability to modulate the sample structure at the atomic level[4].

Mn_3Sn is a non-collinear kagome antiferromagnet that has shown large anomalous hall effect [6, 7] and additional advantages such as zero stray field, high precession frequency, and small damping coefficient [8]. Fig. 1(a) shows the reproduced 2D crystal model of Mn_3Sn consisting of a kagome lattice with an ABAB stacking with a 120-degree spin order[9]. The top two c layers are shown where 1st layer atoms are solid blue (Mn) and red (Sn) and 2nd layer atoms are faded blue (Mn) and faded red (Sn) [21]. In this model, the Sn-Sn a-spacing is shown as 5.665Å. The Mn-atoms sit at the rhombus unit cell center and edge centers and can also be viewed as an Mn hexagon centered at every Sn lattice site.

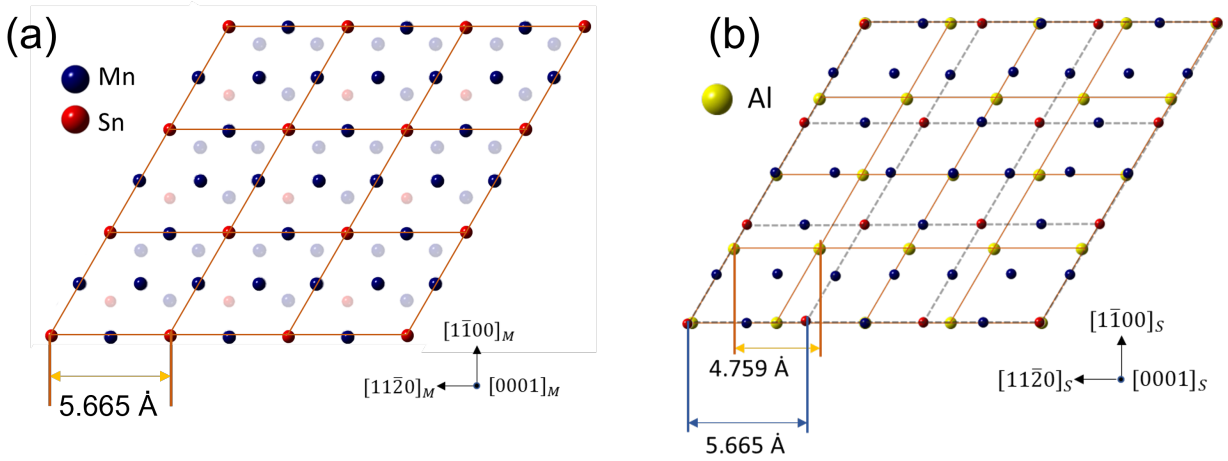

FIG. 1: (a) 2D-model of c-plane Mn_3Sn (b) Overlay of Mn_3Sn on $Al_2O_3(0001)$.

Nakatsuji *et al.* reported that Mn_3Sn single crystal growth using the arc melting method gave a large AHE of 20 Ω^{-1} cm^{-1} at room temperature and more than 100 Ω^{-1} cm^{-1} at low temperatures, reaching the same order of magnitude as compared to some ferromagnetic metal such as Fe, Co or Ni [5]; they observed that the weak ferromagnetic moment of 0.002 Bohr magneton per Mn atom could be switched with a small magnetic field of around 100 Oe [6]. Furthermore, Matsuda *et al.* observed a large anomalous Hall conductivity at THz frequencies at room temperature for Mn_3Sn (0001) deposited on SiO_2. They further showed the temperature dependence on the breaking/recovery of spin textures[10]. Reichlova *et al.* observed magnetic contrast in c-oriented Mn_3Sn grown on MgO (111) using a magnetic imaging technique based on a laser-induced local thermal gradient. They also provided an algorithm to prepare well-defined domain patterns at room temperature based on the heat-assisted recording principle [11]. Ikeda *et al.* reported epitaxial growth of c-plane oriented Mn_3Sn on MgO (111) using sputtering at room temperature. After the growth, the film was annealed at 500 °C to promote crystallization, after which the film was capped with a Ta layer. They further reported that the cross-sectional transmission electron microscope (TEM) indicated that the film was crystallized but not atomically flat [12].

Figure 1(b) shows the direct overlay of an Mn_3Sn (0001) crystal lattice on an Al_2O_3 (0001) lattice. As seen, there is a large lattice mismatch of 19 % and many authors, in

order to get a better lattice match and improve the film quality, have used a variety of different buffer layers. For example, Cheng *et al.* grew a Pt(111) buffer layer on the *c*-oriented sapphire substrate followed by *in-situ* growth of Mn_3Sn using off-axis sputtering. They reported the topological Hall effect (THE) over a temperature range from -63 °C to $+92$ °C by tuning the thickness of the Mn_3Sn films [13]. The presence of THE was likely due to the Dzyaloshinskii-Moriya interaction (DMI) at the Mn_3Sn/Pt interface [13]. Higo *et al.* reported a large anomalous Hall effect (AHE) at room temperature on a single phase Mn_3Sn film grown on a Si buffer layer on SiO_2 by sputter deposition[9].

In this work, the goal is to explore the interfacial structure and crystallinity for direct growth of Mn_3Sn (0001) films on Al_2O_3 (0001) without buffer layers using molecular beam epitaxy (MBE). The material is deposited at 524 ± 5 °C on *c*-plane sapphire substrates and monitored both *in-situ* using reflection high energy electron diffraction (RHEED) and subsequently *ex-situ* using x-ray diffraction (XRD), scanning transmission electron microscopy (STEM), Rutherford backscattering (RBS) and other measurements. We determine the epitaxial film-substrate orientation relationships and crystal models for the film and substrate. We also carefully analyze the lattice parameters as a function of thickness and discuss the strain in the samples. First-principles calculations were performed to investigate and determine the structural atomic arrangement in the first stages of the Mn_3Sn growth process. The surface formation energies formalism was employed to study the thermodynamic stability of the structures.

EXPERIMENTAL

The sample was deposited in a custom-designed ultra-high vacuum (UHV) MBE chamber equipped with Mn and Sn effusion cells (SVT Associates), a quartz-crystal thickness monitor (Inficon STM-2 with internal crystal oscillator), and an RHEED system (STAIB Instruments). The chamber vacuum is maintained with a base pressure in the 10^{-8} to 10^{-9} Torr range using a UHV Cryoplex 8 cryopump on a 10-inch CF flange (Trillium). The RHEED data is acquired using a kSA-400 RHEED data acquisition system (k-Space Associates, Inc.). Crystalline Mn_3Sn films were deposited on commercially available Al_2O_3 (0001) substrates which are single-side polished and grown by the Czochralski method with a miscut of $\pm \frac{1}{2}^\circ$ and surface roughness $R_A < 5$ Å (MTI Corporation). The (0001) substrates

are cleaned using solvents (acetone and isopropanol) in an ultrasonicator and then mounted on 3-inch bayonet-style sample blocks and introduced into the MBE chamber where they are annealed at 1000 ° C for 60 mins on a custom MBE growth stage having a graphitic heater and built-in thermocouple (SVT Associates). The temperature (read out by a Eurotherm 2416 temperature controller) was calibrated using a Fluke single-color pyrometer (model number E2MH-F0-V-0-0), using a wavelength of 1.6 μm, emissivity at 0.7, transmissibility at 0.93 and has a focus range 7.5 to 12". After the substrate annealing, the substrate temperature is lowered to the deposition temperature.

Before every experiment, the source fluxes were checked using the *in-situ* quartz crystal thickness monitor (TM) to determine the ratio of Mn: Sn that would be used for the experiment. The sample was deposited at 524 $\pm$ 5 °C for 90 mins, which ideally gives $\sim$ 200 nm thick film (three samples were grown in total). The film deposition is monitored using RHEED with an incident electron beam energy of 20 keV, providing information on crystalline quality and the *in-plane* lattice parameter. Once the sample is removed from the MBE chamber, it is investigated using XRD to determine the crystal structure and the *out-of-plane* lattice parameter. To confirm the thickness and composition of the grown films, we measured them using RBS.

A Thermo-Fisher Xe plasma G4 dual-beam focused ion beam (FIB) was used for *in-situ* FIB lift-out preparation for the transmission electron microscopy (TEM) study with the final beam condition setting as 5 keV and 10 pA beam current to reduce the FIB damage. Those conditions were also used for SEM imaging. For element maps, Thermo-Fisher Talos F200 TEM with four 30 mm^2 SSD X-ray detectors attached was used and was operated in scanning transmission electron microscopy (STEM) and conventional TEM mode, respectively. A JEOL JEM-3100R05 with double aberration correctors was used for high-resolution STEM imaging which gave a spatial resolution better than 0.1 nm. When operated in STEM mode using the two TEMs, high-angle annular dark-field (HAADF), low-angle annular dark-field (LAADF), and bright-field images were collected simultaneously.

THEORETICAL

In order to study the first stages of Mn_3Sn growth on sapphire, first-principles calculations are carried out based on the density functional theory (DFT) as implemented in the

VASP package [14]. Exchange-correlation energies were treated in the generalized gradient approximation (GGA) by the Perdew-Burker Ernzerhof (PBE) [15]. The interaction between the valence electrons and the core was described with the PAW pseudopotential [16]. Plane waves are used to expand the valence Khon-Sham states with a cut-off energy of 520 eV. The atoms were relaxed within the threshold of the forces of 0.01 eV/Å, while the energy conversion criterion is set to be 10^{-5} eV. The Brillouin zone was sampled by using an 8×8×1 Monkhorst-Pack[17].To model the growth process, the super-cell method is used with an empty space of 17.5 Åadjacent slabs was used to avoid inter-slab interactions. The lattice parameter of the substrate $(0001)_S$ was taken from the experimental values, a= 4.759 Å and c= 12.992 Å with a surface periodicity of (1×1). Additionally, the non-collinear behavior of Mn_3Sn is considered in all calculations.

RESULTS

Before starting the deposition, the fluxes for Mn and Sn were measured, using the TM, to be 1.5×10^{14} atoms/cm^{2}s and 4.8×10^{13} atoms/cm^{2}s respectively. This gave a ratio of $J_{Mn}/J_{Sn} = 3.1$, which was used to deposit the materials at a sample temperature of 524 ± 5 °C. The sapphire substrate was annealed, and the resulting RHEED patterns are shown in Figs. 2(a) and 2(b).

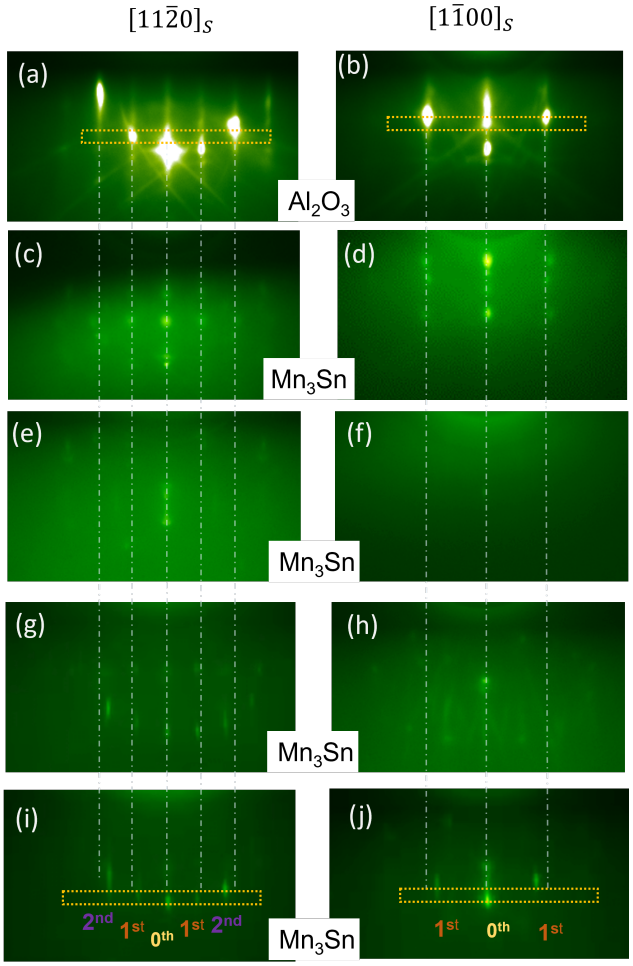

FIG. 2: RHEED patterns of Al_2O_3 and growth of Mn_3Sn at 524 $\pm$ 5 °C where the yellow boxes show where the line profiles are taken and the dashed lines indicate the positions of the sapphire streaks; (a-b) annealed Al_2O_3; (c-d) immediately after opening the shutter; (e-f) after 90 mins of Mn_3Sn growth at 524 °C; (g-h) Mn_3Sn next day at 300 K; (i-j) Mn_3Sn after 5 days at 300 K.

Later, the growth stage temperature was lowered to the deposition temperature, the Mn and Sn effusion cell shutters were opened simultaneously and the RHEED patterns quickly turned spotty as shown in Figs. 2(c) and 2(d). This point pattern indicates island growth and closely follows the *in-plane* spacing of the annealed Al_2O_3. In the initial stage of growth, the surface is strained to the substrate as seen in the RHEED pattern where the *in-plane* dot spacing matches the substrate spacing.

This point pattern is visible until a thickness $\sim$ 15 nm, after which the RHEED pattern

begins gradually fading towards a non-crystalline pattern. Eventually, the growth reaches the patterns shown in Figs. 2(e) and 2(f) after 90 minutes. After the completion of growth, the surface is non-crystalline, which crystallizes once the surface is allowed to anneal at room temperature over a few days (annealing at elevated temperatures for shorter period was tried, which resulted in a dot RHEED pattern,suggesting a rough surface).

Figs. 2(g) and 2(h) shows the RHEED pattern the next day at room temperature, indicating a high degree of crystallinity. The crystallinity is clearly measurable by the streak pattern, and no polycrystallinity is observed. Furthermore, the patterns appeared more and more crystalline after five days, as seen in Figs. 2(i) and 2(j). Similar RHEED patterns to those shown in Figs. 2(i) and 2(j) were seen at 60-degree azimuthal intervals of the sample. This indicates that the film has a 6-fold crystalline symmetry.

Line profiles were taken across Figs. 2(a) and 2(b) for annealed Al_2O_3 and Figs. 2(i) and 2(j) for Mn_3Sn, as shown in Fig. 3, to derive the lattice constant. We see that the streak spacing is narrower for the Mn_3Sn as compared to the Al_2O_3 in both directions, which indicates that the lattice parameters of Mn_3Sn are larger than those of Al_2O_3 in the *in-plane* directions. Note that the additional small peaks in the sapphire line profile along the $[1\bar{1}00]_S$ direction are due to Kikuchi lines, therefore they are not considered in the calculations.

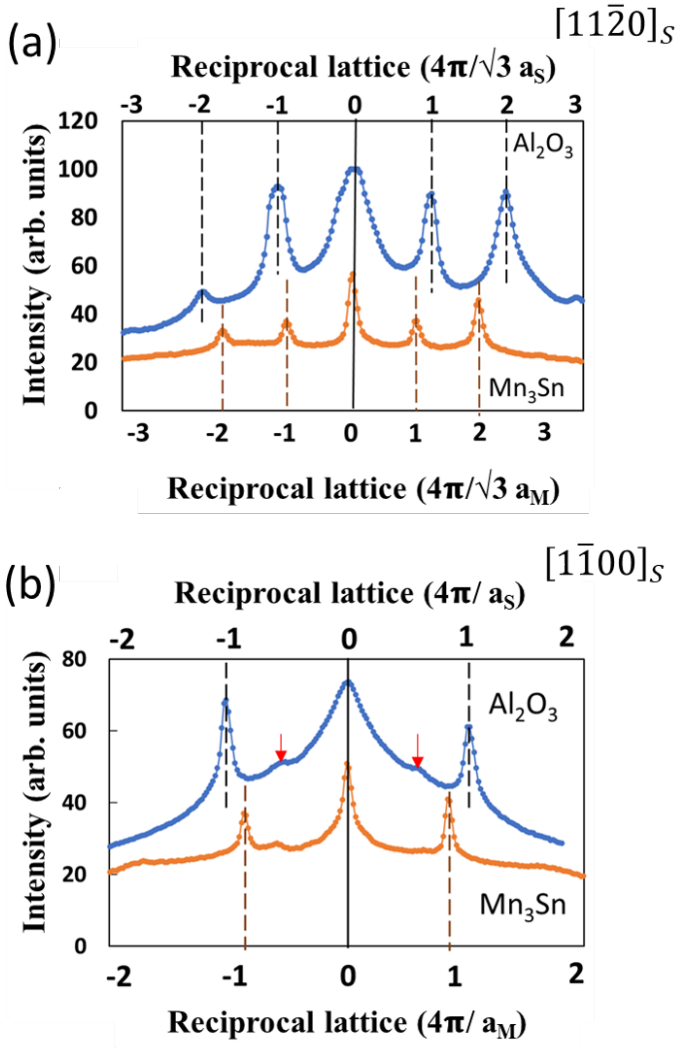

FIG. 3: Line profile of the RHEED patterns for annealed Al_2O_3 and Mn_3Sn in both (a) $[11\bar{2}0]_S$ and (b) $[1\bar{1}00]_S$ directions. The red arrows point to small peaks that are due to Kikuchi lines.

Since Al_2O_3 is a hexagonal structure, the primary streak spacing along $[11\bar{2}0]_S$ is $\frac{4\pi}{\sqrt{3}a_S}$ where we define $a_S = a_{Al_2O_3}$; along $[10\bar{1}0]_S$ the RHEED streak spacing is $\frac{4\pi}{a_S}$. Therefore, the streak spacing of the two azimuths differs by a factor of $\sqrt{3}$. From the RHEED patterns for the Mn_3Sn, we can see that the same $\sqrt{3}$ ratio exists. Therefore, we conclude that the Mn_3Sn surface is hexagonal and thus is the *c*-plane. As such, the *in-plane* lattice parameter of Mn_3Sn corresponding to the primary streak spacings can be calculated using the equation:

$$a_M = a_S \times \frac{W_S}{W_M}, \tag{1}$$

where W_S and W_M are the first order streak spacings of Al_2O_3 and Mn_3Sn respectively, and a_M and a_S are the *in-plane* lattice constants of Mn_3Sn and Al_2O_3 respectively. Using a_S = 4.759 Å, we calculated $a_M = 5.672 \pm 0.012$ Å along $[11\bar{2}0]_S$ and $a_M = 5.688 \pm 0.011$ Å along $[10\bar{1}0]_S$. The average lattice constant is therefore $a_M = 5.680 \pm 0.012$ Å, which is in excellent agreement with bulk Mn_3Sn value of 5.665 Å [9, 18]. The small difference of 0.015 Å (0.26%) is close enough to 1 sigma that the RT-annealed film seems to be fully relaxed.

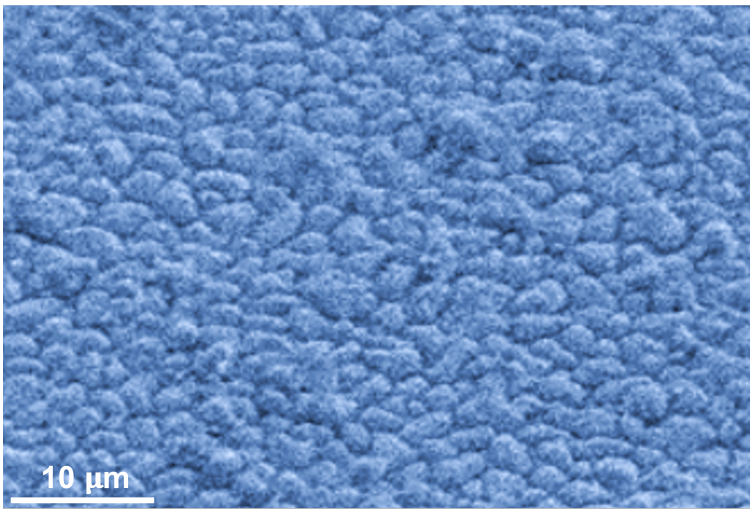

FIG. 4: SEM image of the deposited sample. HFW (or field of view) = 41.4 μm.

STEM was carried out to characterize the morphology of the sample and elemental mapping was carried out. Figure 4 shows the SEM image of the sample. We can see that the surface appears to be lumpy with 3D structures present having a characteristic size of several micrometers. The cross-sectional STEM in Fig. 5(a) shows the presence of 3D domes with an average height of $\sim$ 225 nm. There are also some smaller-sized 3D domes in between the larger ones. This indicates that a process of Ostwald ripening has most likely occurred. Additionally, Mn and Sn elemental mapping is shown in Fig. 5(b) and Fig. 5(c) respectively, where there appears to be a uniform composition of Mn and Sn within the domes. To get a numerical Mn: Sn ratio, we performed RBS on this sample, resulting in a global average (over the RBS spot size of 1×2 mm^2) of Mn: Sn = 2.47:1 and the thickness of the film was calculated to be $\sim$ 170 nm. It is surprising that our a_M value is so close to the expected value despite the stoichiometry of the sample being much less than 3:1. Furthermore, the grown surface is Sn rich which is because of the low sticking coefficient of Mn at this growth temperature. These results show that in future growth, a higher flux ratio needs to be used

in order to reach the desired stoichiometry.

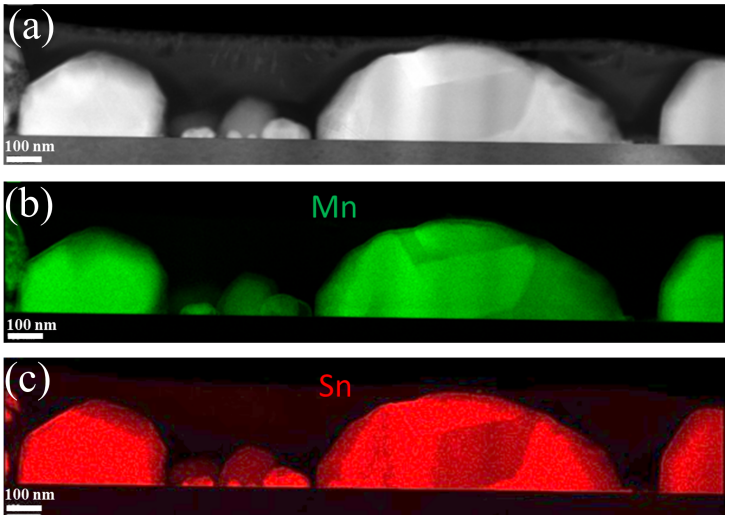

FIG. 5: STEM elemental mapping indicating the composition of Mn and Sn for the sample. (a) is the dark field reference image taken before the elemental mapping; (b) and (c) show the elemental composition of Mn_3Sn in that region.

To further explore the crystalline orientation of the film, XRD was carried out as shown in Fig. 6. To calculate the d-spacing, the average $K\alpha$ wavelength of $\lambda = 1.542$ Å is used. In order to obtain the most accurate d-spacing values for the sample, we calibrated the spectrum by forcing the sapphire 0006 peaks to lie at precisely $2\theta = 41.72°$, which gives a d-spacing = 2.165 Å, resulting in $c_S = 6d = 12.991$ Å, the most precise known value for c_S at 300 K [19]. Then, the first largest Mn_3Sn peak lies at 39.92° and gives a d spacing = 2.259 ± 0.012 Å and therefore we get $\bar{c}_M = 4.517$ Å ± 0.011 Å. The standard deviation of the mean ($\bar{c}_M$ value) is derived from the standard deviation of the distribution (or a single value) by dividing the latter by $\sqrt{N}$ [20]. The mean value is smaller by 0.3% compared to the c value reported by Higo *et al.* and by Tomita *et al.* = 4.531 Å [9, 18]. The difference is much greater than the estimated uncertainty; therefore, this is a real difference, and it implies that the measured *out-of-plane* lattice constant is smaller for this sample having a 2.47:1 Mn-to-Sn atomic ratio, as compared to the value reported for the 3:1 ideal ratio. It is consistent with a lattice constant arising from the Mn deficiency, but it is interesting that a 17.7% Mn deficiency results in only a 0.3% change in the c-value.

Since the Mn_3Sn 0002 peak is the dominant Mn_3Sn peak, this sample is predominantly c-

oriented. However, the XRD spectrum in Fig. 6 also shows several additional much smaller peaks including e.g. Mn_3Sn $11\bar{2}0$, Mn_2Sn 0002, and some others.

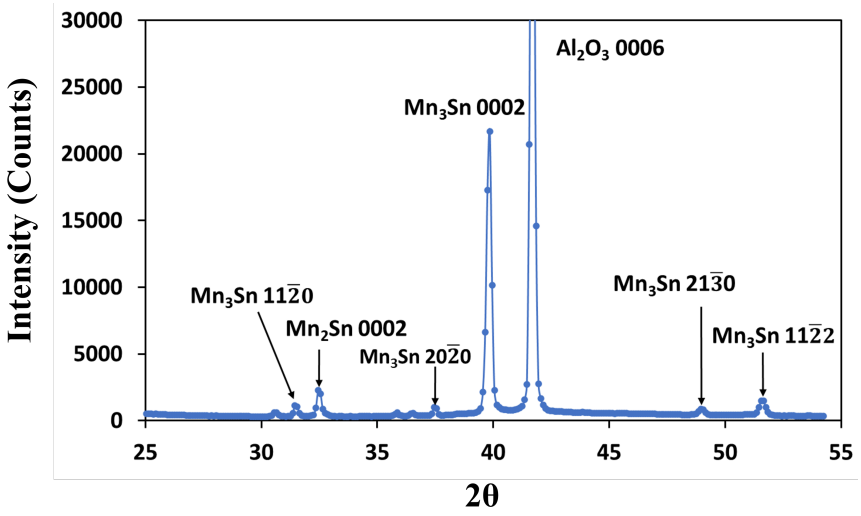

FIG. 6: X-ray diffraction pattern of Mn_3Sn/Al_2O_3 (0001) deposited at 524 ± 5 °C. X-rays are Cu K_α. The sapphire 0006 peak intensity is 55338 counts but is truncated to zoom in on the manganese-tin peaks.

Furthermore, the substrate-film orientation relationship is found to be $[11\bar{2}0]_M \parallel [11\bar{2}0]_S$, $[1\bar{1}00]_M \parallel [1\bar{1}00]_S$, and $[0001]_M \parallel [0001]_S$ from the RHEED as the streak spacing ratio between $[11\bar{2}0]_S$ and $[1\bar{1}00]_S$ is the same $\sqrt{3}$ for both Mn_3Sn as well as sapphire. Using these orientation relationships, it's possible to overlay the Mn_3Sn model onto a sapphire substrate model to see how the Mn- and Sn-atoms will align with the Al-atoms. Based on the RHEED patterns shown in Figs. 2(c) and 2(d), in which the Mn_3Sn lattice spacing matches initially the sapphire Al-Al spacing, therefore in the model shown in Fig. 7, we show a pseudomorphic overlay in which a single Mn_3Sn layer is aligned on top of an Al_2O_3 bilayer.

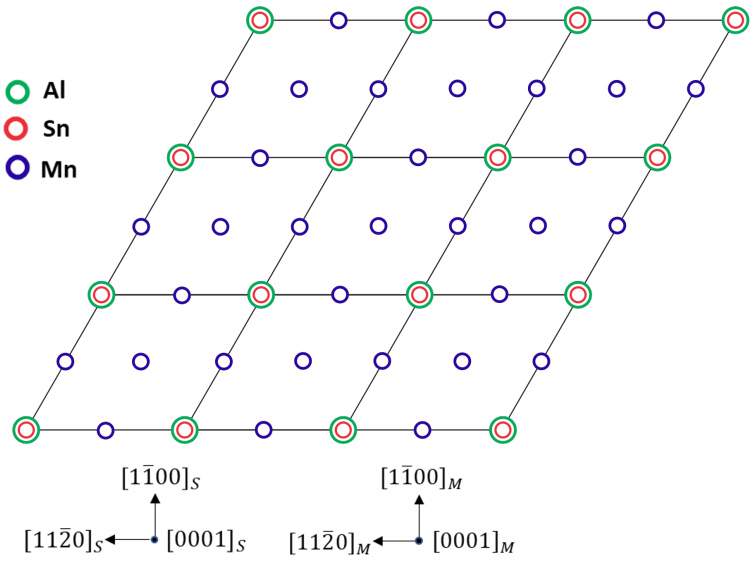

FIG. 7: Pseudomorphic overlay of Mn_3Sn on c (0001) Al_2O_3 is shown.

The model shown in Fig. 7 explains the observed RHEED data at the initial stage of growth in which we see an approximately pseudomorphic growth with a large amount of strain. The average lattice constant calculated from Figs. 2(c) and 2(d) is 4.575 ± 0.013 Å which when compared to the reported a_M = 5.665 Å indicates a compressive strain of 19.2 %. This strain then releases as additional layers are deposited which then leads to the formation of faceted dome-like structures. This behavior is similar to that observed in Ge growth on silicon substrates [22, 23].

Table I summarizes the detailed results of the calculated lattice parameters from RHEED, composition, and thickness from RBS. The XRD results show the list of all the lattice orientations present in the film along with their 2θ values. The relative intensity for a given Mn_3Sn peak was calculated by normalizing the peak's intensity to the sum of all the Mn_3Sn peak intensities, as shown in the table. The results shown in Table 1, therefore, indicate that the grown film is predominantly (79 % relative intensity) c-plane Mn_3Sn with a 2.47:1 Mn: Sn ratio.

THEORETICAL STUDY

Considering the experimental results, we have modeled the Mn_3Sn first stages of growth on Al_2O_3 (0001). Calculations were carried out to first understand the Mn-only and Sn-only

XRD				RHEED	RBS
2θ	Peak label	Relative Intensities	Lattice parameter	Average lattice parameter	Composition and thickness
31.62	Mn_3Sn $11\bar{2}0$	4%			
32.62	Mn_2Sn 0002	7%	Mn_3Sn 0002:		Mn:Sn = 2.47:1
37.62	Mn_3Sn $20\bar{2}0$	3%	c = 4.517 ±	5.680 ± 0.012 Å	Thickness ∼ 170 nm
39.92	Mn_3Sn 0002	79%	0.011 Å		
49.12	Mn_3Sn $21\bar{3}0$	3%			
51.72	Mn_3Sn $11\bar{2}2$	4%			

TABLE I: Summary of the results of the sample deposited at 524 ± 5 °C. Relative intensities of different orientations of Mn_xSn show predominant c-plane Mn_3Sn orientation.

adsorption on sapphire cases, which are discussed in the Supplementary material. In these calculations, the L3 site (obtained when the ad-atom is placed on top of the third layer aluminum, see Supplementary) was the most stable in the Mn-only and Sn-only adsorption cases. On the other hand, depositing two or four monolayers (ML) of Mn_3Sn on sapphire resulted in the H3 site (obtained when the ad-atom is placed on top of the second layer of oxygen) being the most stable configuration. In this configuration, the Sn atoms are bonded with the first layer of oxygen atoms.

The optimized structures are depicted in Fig. 8 where (a),(b) correspond to the two Mn_3Sn layers case and (c),(d) correspond to the four Mn_3Sn layers case. The bond length between Sn and sapphire (O) is 2.49 Å. It is noted, as displayed in Fig. 8, that in both the 2 and 4 ML cases, Mn_3Sn layers do not exhibit a perfect kagome structure. However, if we view the Mn_3Sn structure in the top view, as shown in Figs. 8(b) and 8(d), we find that Mn still has a triangular structure with a 3-point basis in each layer, implying Mn_3Sn is growing in the kagome structure with vertical and lateral displacements away from the ideal bulk-like Mn_3Sn structure. This behavior is attributed to substrate-induced compressive strain, and therefore the interatomic distances within the kagome plane become inequivalent. Hence, the presence of displacements causes the Mn atoms in the kagome structure to be highly distorted, and the Sn atoms do not cohabitate within the Mn layers, as seen in the side views [Figs. 8(a) and 8(c)]. From the above explanation, the growth of Mn_3Sn is initialized

by forming a displaced kagome structure which explains the crystalline spot-like RHEED pattern shown in Figs. 2(c) and 2(d).

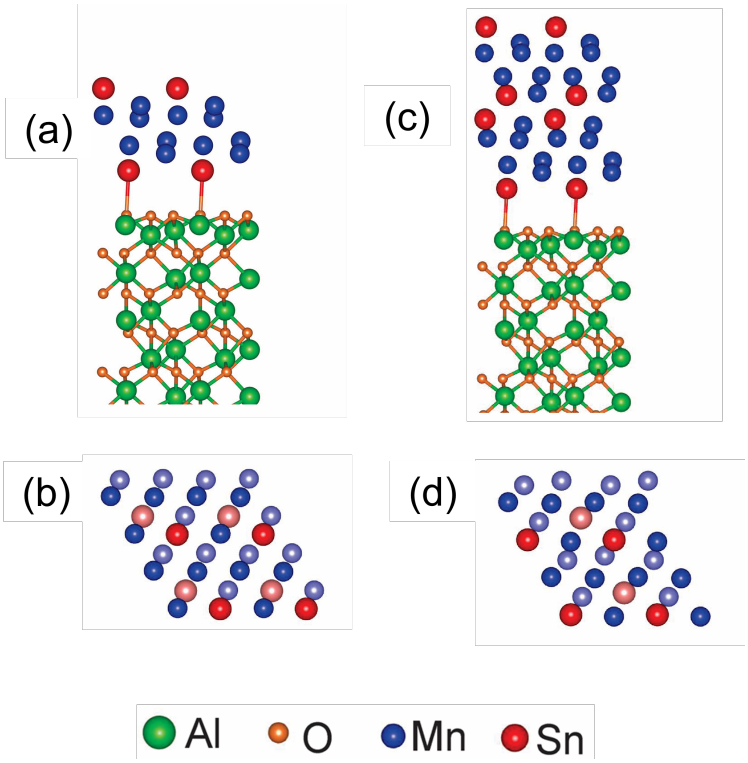

FIG. 8: (a), and (b) is the side and top view for the two bilayers Mn_3Sn case on sapphire, respectively. (c) and (d) is the side and top view for the four bilayers Mn_3Sn case on sapphire, respectively. The faded atoms correspond to the bottom layer.

In order to determine the stability of the different configurations, the surface formation energy (SFE) formalism has been employed since each model has a different number of atoms by cell.[25] The SFE can be written in the following form:

$$E_{SF} = E_{slab} - E_{ref} - n_{Mn}\mu_{Mn} - n_{Sn}\mu_{Sn} \tag{2}$$

Here E_{SF} is the surface formation energy of the system at hand, E_{slab} is the system total energy of each model, n_i and μ_i are the number of atoms, and the chemical potential of the i^{th} species, respectively. The SFE is independent of the number of atoms but depends on the chemical potentials of the structural components. Therefore, the SFE is plotted as a function of the Mn chemical potential, with a lower limit of $\mu_{Mn} = \mu_{Mn}$ (bulk) (namely Mn-rich conditions) and an upper limit of $\mu_{Mn} = \mu_{Mn}$ (bulk)$-\Delta$H (corresponding to Mn-poor

conditions or Sn-rich conditions) where ΔH is the enthalpy of formation of the Mn_3Sn bulk structure with a value of $\Delta H = -0.15$ eV. The Mn and Sn chemical potentials are obtained by modeling the $\alpha-$Mn phase with 58 atoms per unit cell and the $\beta-$Sn phase with 4 atoms per unit cell, respectively. The results are illustrated in Fig. 9.

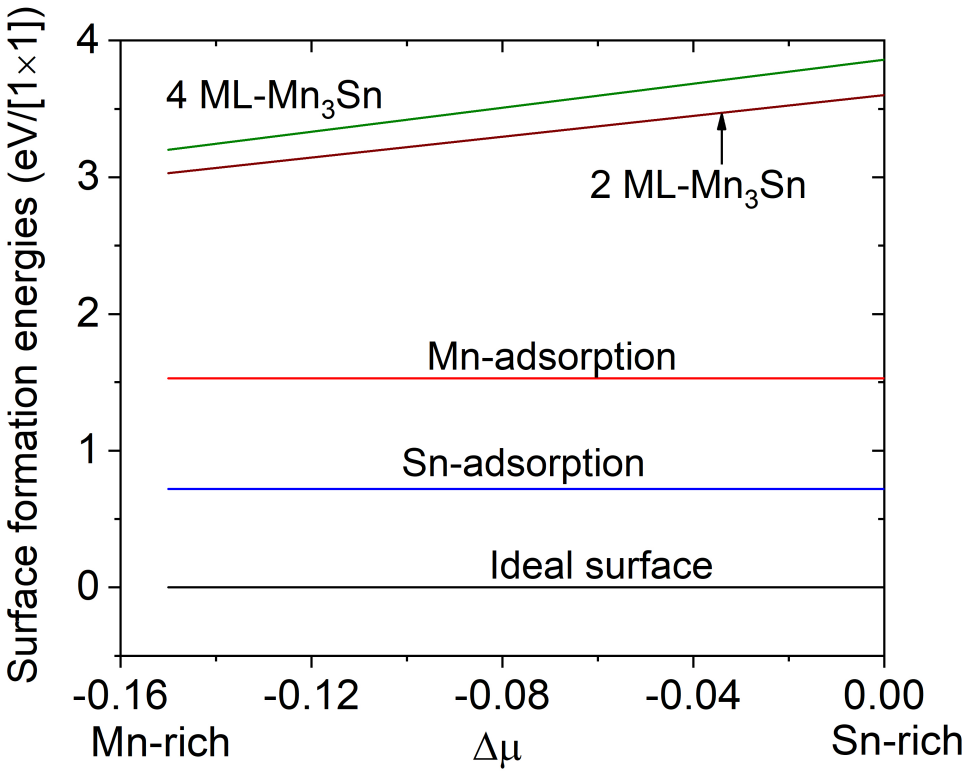

FIG. 9: Surface formation energies (SFE) for the most representative structures.

According to the results as seen in Fig. 9 for the Sn or Mn-only adsorption cases, the Sn adsorption is more energetically favorable than the Mn adsorption. On the other hand, the SFE's for two and four Mn_3Sn layer models are much higher, with the 4 ML model being slightly higher in energy as compared to the 2 ML model. This suggests that with increasing Mn_3Sn thickness, the Mn_3Sn kagome lattice does not increase in stability. Therefore, the theoretical results suggest that in the first stages of Mn_3Sn growth on sapphire (0001), Mn_3Sn does not form a stable and perfect kagome structure, consistent with the observed RHEED patterns shown in Figs. 2(c) and 2(d).

As growth continued out to the final thickness, the RHEED pattern became more and more featureless (blank screen), as shown in Figs. 2(e) and 2(f). This is modeled theoretically

as a semi-amorphous state. A similar behavior was observed previously in the case of ultra-thin GeTe thin films.[24].

More importantly, the displacements away from the equilibrium kagome lattice structure which we see theoretically at the initial stages of c-plane growth on sapphire may be of significance to transport behavior. Very recently, Berthold et al. reported the discovery of small displacements away from equilibrium seen in their Mn_3SnN thin films, which they discuss in terms of the relevance to the observed anomalous Hall effect. Furthermore, they also showed that the Mn displacements away from their equilibrium positions decrease with increasing film thickness [26]. This is apparently what we also observe, that the displacements away from equilibrium decrease as the number of atomic layers increases up to a limiting thickness, and the $(0001)_M$ thin film relaxes from the compressive strain toward that of the bulk behavior ($a_M = 5.680$ and a perfect kagome structure).

CONCLUSIONS

In conclusion, we performed MBE growth of Mn_3Sn directly on *c*-plane sapphire (0001) substrates, and as we have shown, the material followed the substrate crystal lattice. The sample was grown at 524 ± 5 °C which led to a predominantly *c*-plane oriented film. The average *in-plane* lattice constant calculated using RHEED was 5.680 ± 0.21 % and is within 0.27 % of the reported bulk value of 5.665 Å [9, 18], and therefore is in good agreement to within almost 1 sigma. From the XRD results, the *out-of-plane* lattice constant was calculated to be 4.517 ± 0.24 % and is within 0.30% of the reported bulk value of 4.531 Å [9, 18], and therefore is in good agreement to within almost 1 sigma. Furthermore, the STEM results indicate the presence of dome-like structures which may be responsible for relaxing the strain from the sapphire substrate. More studies need to be carried out by either changing the growth protocol, or by choosing substrates with a lower lattice mismatch, for example using $LaAlO_3$ with a $6\% \; in-plane$ lattice mismatch with Mn_3Sn.

Additionally, the initial stages of growth were investigated by density functional theory to compare with the experimental results. The results show that a displaced kagome structure of Mn_3Sn is formed for two or four atomic layers due to the substrate strain. The SFE shows that the Mn_3Sn kagome structure is not thermodynamically stable in these initial stages of growth with a separation of the Mn and Sn sub-lattices which explains the observable

RHEED pattern. More studies will be required to understand how the structures at the initial stages of growth transition to the kagome structure at large layer thicknesses and whether or not the first few layers form a wetting layer prior to the formation of the dome-like structures.

The authors acknowledge support from the U.S. Department of Energy, Office of Basic Energy Sciences, Division of Materials Sciences and Engineering under Award No. DE-FG02-06ER46317. N.T. thanks DGAPA-UNAM project IN105722 and Conacyt grant A1-S-9070 for partial financial support. Calculations were performed in the DGCTIC-UNAM Supercomputing Center, project LANCAD-UNAM-DGTIC-051. J.C.H. thanks the Nanoscale and Quantum Phenomena Institute and the Department of Physics and Astronomy at Ohio University for partially funding his visit to Ohio University in Fall 2022. The authors would like to thank Dr. Eric Stinaff and his students for back-coating the sapphire substrates. The authors would like to thank Mr. Greg Secord from Fluke Process Instruments for help with the optical pyrometer measurements using the Fluke pyrometer model E2MH-F0-V-0-0 and in carrying out the sample temperature calibration.

CONFLICT OF INTEREST

The authors have no conflicts of interest to disclose.

DATA AVAILABILITY

The data supporting this study's findings are openly available in Zenodo at [DOI to be added]

[1] L. Ye, M. Kang, J. Liu, F-V Cube, C.R Wicker, T. Suzuki, C. Jozwiak, A. Bostwick, E. Rotenberg, D.C.Bell, L.Fu, R.Comin, and J.G. Checkelsky, "Massive Dirac Fermions in a Ferromagentic Kagome Metal", Nature **555**, 638 (2018).

[2] M. Kang, S. Fang, L. Ye, H. C. Po, J. Denlinger, C.Jozwiak, A.Botswick, E. Rotenberg, E. Kaxiras, J.G. Checkelsky, and R. Comin, "Topological Flat Bands in Frustrated Kagome Lattice CoSn", Nature Communications **11**, 1 (2020).

[3] D. Hong, C. Liu, H-W Hsiao, D. Jin, J.E. Pearson, J-M Zuo, and A.Bhattacharya "Moelcular Beam Epitaxy of the Magnetic Kagome Metal FeSn on $LaAlO_3$ (111)", AIP Advances **10**,105017 (2020).

[4] S. Cheng, B. Wang, I. Lyalin, N. Bagués, A.J. Bishop, D.W. McComb, and R. Kawakami, "Atomic Layer Epitaxy of Kagome Magnet Fe_3Sn_2 and Sn - modulated Hetereostructures", APL Mater. **10**, 061112 (2022).

[5] N.Nagaosa, J.Sinova, S.Onoda, A.H. MacDonald and N.P. Ong, "Anomalous Hall effect ", Rev.Mod.Phys., **82**, 1539 (2010).

[6] S. Nakatsuji, N. Kiyohara and T. Higo , "Large anomalous Hall effect in a non-collinear antiferromagnet at room temperature", Nature **527**, 212 (2015).

[7] J.M. Taylor, A. Markou, E. Lesne, P. K. Sivakumar, C. Luo, F. Radu, P. Werner, C. Felser, and S. S. P. Parkin, "Anomalous and topological Hall effects in epitaxial thin films of the noncollinear antiferromagnet Mn_3Sn", Phys. Rev B, **101**, 094404 (2020).

[8] J-Y Yoon, Y. Takeuchi, S. DuttaGupta, Y. Yamane, S. Kanai, J. Ieda, H. Ohno, and S. Fukami , "Correlation of anomalous Hall effect with structural parameters and magnetic ordering in $Mn_{3+x}Sn_{1-x}$ thin films", AIP Advances **11**, 065318 (2021).

[9] T. Higo, D. Qu, Y. Li, C. L. Chien, Y. Otani, and S. Nakatsuji, "Anomalous Hall effect in thin films of the Weyl antiferromagnet Mn_3Sn", Appl. Phys. Lett. **113**, 202402 (2018).

[10] T. Matsuda, N. Kanda, T. Higo, N.P. Armitage, S. Nakatsuji and R. Matsunaga, "Room-temperature terahertz anomalous Hall effect in Weyl antiferromagnet Mn_3Sn thin films". Nature Communications **11**,8 (2020).

[11] H. Reichlova1, T. Janda, J. Godinho, A. Markou, D. Kriegner, R. Schlitz, J. Zelezny, Z. Soban, M. Bejarano, H. Schultheiss, P. Nemec, T. Jungwirth, C. Felser, J. Wunderlich and S.T.B. Goennenwein, "Imaging and writing magnetic domains in the non-collinear antiferromagnent Mn_3Sn," Nature Communications **10**, 1 (2019).

[12] T. Ikeda, M. Tsunoda, M. Oogane, S. Oh, T. Morita, and Y. Ando, "Fabrication and evaluation of highly c-plane oriented Mn_3Sn thin films," AIP Advances **10**, 015310 (2020).

[13] Y. Cheng, S. Yu, M. Zhu, J. Hwang, and F. Yang, "Tunable Topological Hall effects in noncollinear antiferromagnets Mn_3Sn/Pt bilayers", APL Materials **9**, 051121 (2021).

[14] Hafner, J. "Ab-initio simulations of materials using VASP: Density-functional theory and beyond". Journal of computational chemistry, **29**, 2044-2078 (2008).

[15] Hammer, B. H. L. B., Hansen, L. B., and Nørskov, J. K. "Improved adsorption energetics within density-functional theory using revised Perdew-Burke-Ernzerhof functionals". Physical review B, **59**, 7413 (1999).

[16] Kresse, G., and Furthmüller, J. "Efficient iterative schemes for ab initio total-energy calculations using a plane-wave basis set". Physical review B, **54**, 11169 (1996).

[17] Monkhorst, H. J., and Pack, J. D. Special points for Brillouin-zone integrations. Physical review B, **13**, 5188 (1976).

[18] T. Tomita, M. Ikhlas, and S. Nakatsuji, "Large Nernst Effect and Thermodynamics Properties in Weyl antiferromagnet", JPS Conf.Proc.**30**, 011009 (2020).

[19] M. Lucht, M. Lerche, H.-C. Wille, Yu. V. Shvyd'ko, H. D. Rüter, E. Gerdau, and P.Becker, "Precise measurement of the lattice parameters of sapphire in the temperature Range 4.5 K - 250 K using the Mössbauer wavelength standard", J. Appl. Cryst. **36**, 1075 (2003).

[20] Philip R. Bevington, "Data reduction and error analysis for the physical sciences", McGraw-Hill Book Company, Lib. of Congress Cat. card No. 69-16942, p. 71 (copyright 1969).

[21] Images and video generated using CrystalMaker®: a crystal and molecular structures program for Mac and Windows. CrystalMaker Software Ltd, Oxford, England (www.crystalmaker.com)

[22] H.Ye and J.Yu, "Germanium epitaxy on silicon". Sci.Technol.Adv.Mater.,**15**, 024601 (2014).

[23] H.Sunamura, N.Usami and Y.Shiraki, "Island formation during growth of Ge on Si (100): A study using photoluminescence spectroscopy". Appl.Phys.Lett. , **66**, 3024 (1995).

[24] Hilmi, I., Lotnyk, A., Gerlach, J. W., Schumacher, P., and Rauschenbach, B. Influence of substrate dimensionality on the growth mode of epitaxial 3D-bonded GeTe thin films: From 3D to 2D growth, Mater. Des. **168**, 107657 (2019).

[25] Moreno, J. C., Camacho-Garcia, J. H., Ponce-Pérez, R., Sánchez-Ochoa, F., de la Cruz, M. T. R., and Cocoletzi, G. H. Initial stages of the epitaxial growth of AlN on GaN (1 1 1)-(2× 2) surface: Ab-initio studies. Journal of Crystal Growth. **507**, 370-378 (2019).

[26] Rimmler, B. H., Hazra, B. K., Pal, B., Mohseni, K., Taylor, J. M., Bedoya-Pinto, A., ... and Parkin, S. S. Atomic Displacements Enabling the Observation of the Anomalous Hall Effect in a Non-Collinear Antiferromagnet. Advanced Materials. 2209616 (2023).